Towards efficient NFA-based selective near-infrared organic photodetectors: impact of thermal annealing of polymer blends

Q. Eynaud, Y. Avalos Quiroz, T. Koganezawa, R. Sato, N. Yoshimoto, O. Margeat, C. Ruiz, J. Ackermann, Christine Videlot-Ackermann

Towards efficient NFA-based selective near-infrared organic photodetectors: impact of thermal annealing of polymer blends

Q. Eynaud,[a] Y. A. Avalos Quiroz,[a] T. Koganezawa,[b] R. Sato,[c] N. Yoshimoto,[c] O. Margeat,[a] C. M. Ruiz,[d] J. Ackermann,[a] C. Videlot-Ackermann*,[a]

[a] *Aix Marseille Univ., CNRS, CINAM, Marseille, France*
[b] *Industrial Application Division, Japan Synchrotron Radiation Research Institute (JASRI), Sayo, Hyogo 679-5198, Japan.*
[c] *Department of Physical Science and Materials Engineering, Iwate University, Ueda Morioka 020 8551, Japan.*
[d] *Aix Marseille Univ.,Univ. de Toulon, UMR CNRS 7334, IM2NP, Marseille, France*

Abstract

For wavelength-selective photodetection or color discrimination, organic photodetectors (OPDs) can provide significant advantages as solution processability, chemical versatility and functionality. To eliminate the need for commonly used filters, the development of a narrowing approach that simultaneously achieves a selective detection range of less than 50 nm bandwidth and a spectral response greater than 20%, especially for wavelengths designed in the near-infrared, remains a real challenge. Herein, we demonstrate a bulk-heterojunction (BHJ) organic blend exhibiting a filter-free visible-blind near-infrared light responsive characteristic. An indacenodithienothiophene-based non-fullerene acceptor (NFA) of the ITIC family incorporating fluorine atoms, namely ITIC-4F, is mixed with PM6 donor polymer to form ultra-thick active layers in OPDs. A systematic comparison between inverted versus normal architectures was performed using different pairs of hole and electron extraction layer materials. Depending on the thermal annealing temperature of PM6:ITIC-4F blends (from 100°C up to 200°C), distinct light responses were observed. While the spectral response of normal structures changes from narrow to broadband with the temperature, inverted structures improve their spectral tuning. A detailed analysis of structure and morphology of blends upon thermal annealing was performed by atomic force microscopy (AFM), contact water angle (CWA) measurement, Raman analysis and 2D grazing-incidence X-ray diffractometry (2D-GIXRD). The transport properties of electrons and holes were further investigated in blends following a Space-Charge-Limited Current (SCLC)

protocol. We found a marked misbalance between hole and electron mobility values at 200°C together with highly crystalline films. As a result, the optimized OPD exhibits a high-selective spectral response following the charge collection narrowing (CCN) principle with an external narrowband quantum efficiency of 24.5% and a bandwidth of 42 nm centered at 807 nm. A specific detectivity as high as ~6×10^{12} Jones is also achieved due to a low dark current density.

Introduction

Photodetectors, one of the most important types of optoelectronic devices, are transducers that change one of their characteristics when light passes through them. The operating principle of most modern photodetectors is based on electrical responses by converting photons into charge carriers and producing a change in voltage or current in electrical circuits. Photodetectors have a wide range of applications, both in industry and in our daily lives as environmental monitoring; biomedical imaging, surveillance, machine vision and sensing. In recent years, solution-processable semiconductors, e.g., organic semiconductors, quantum dot based ones, and organic-inorganic hybrid perovskites, have emerged as promising candidates for photodetection.[1-7] These novel photodetectors have demonstrated excellent device flexibility, solution processability, chemical versatility, and functionality.[8-11] Specifically, organic photodetectors can be fabricated via various printing techniques through wet chemistry, such as spray coating, spin coating, inkjet printing, and roll-to-roll printing. Particularly, the fabricated organic photodetectors (OPDs) based on bulk heterojunctions (BHJs) have shown exceptional performance metrics, which are on a par with the established Si technologies.[3,12,13]

Organic semiconductors are typically used as active layers in solar cells because of their broadband absorption range that allows for maximum sunlight harvesting. By modifying the chemical structure, a large diversity of materials is accessible adapting the spectral response range. The most efficient solution-processable organic solar cells are based on BHJ blends of an electron donating conjugated polymer (p-type semiconductor) and a n-type material usually represented by fullerene derivatives or more recently non-fullerene acceptors (NFAs).[14,15] As for organic solar cells, a broadband response can be easily achieved in OPDs by using active layer materials with a wide absorption range from UV to NIR. In contrast, narrowband OPDs are difficult to achieve when wavelength-selective photodetection or color discrimination is required

for a wide range of applications, including image capture, machine vision, and security monitoring.

Many strategies to achieve narrowband OPDs have been investigated: (i) using specific materials with intrinsic narrowband photoresponse, (ii) combining bandpass filters with broadband photodetectors, (iii) optimizing the optical structure to achieve the desired narrow absorption for the tunable wavelength range, and (iv) adjusting the desire thickness and manipulating the carrier transport to narrow down the spectral response.[7,16-18] With the latter strategy, the color selectivity in OPDs can be accomplished by manipulating the internal quantum efficiency via charge collection narrowing (CCN).[19-21] The working principle of CCN connects with the wavelength-dependent absorption coefficients on incident photons within the photoactive layer. When the photoactive layer thickness is set to be much thicker than the absorption depth, aspects of electrical signal formation begin to diverge for incident photons with high and low absorption coefficients. According to the Beer-Lambert law, photons whose energy corresponds to the absorption peak of materials will be absorbed near the illuminated surface of the active layer where photo-carrier generation will occur. Due to the low charge mobility and high thickness of active layer, the generated charges tend to recombine before reaching the back electrodes. In contrast, photons with energy close to the absorption tail can penetrate further into active layer and charges can be generated uniformly across the thick film, leading to a more balanced charge collection at the front (illuminated transparent electrode) and back electrodes. Thus, an external quantum efficiency (EQE) response is obtained at the wavelength near the absorption tail. This is ideally reflected in the EQE spectrum by a specific photoresponse and blindness outside this spectral window. Armin *et al.* first developed high-performance CCN OPDs in 2015 using an ultra-thick (2 μm) BHJ active layer.[19] The red-selective and NIR-selective OPDs achieved a narrow full-width at half-maximum (FWHM) of about 90 nm, with a detectivity exceeding 10^{12} Jones. CCN concept is based on the development of photodiode (PD) type OPDs, and strongly depends on the absorption range of the active layer.[20] Meanwhile, the EQE of PD-type OPDs is less than 100% because its working mechanism is similar to that of organic solar cells. The EQE spectra strongly depends on photon harvesting, exciton dissociation, charge carrier transport and collection.

In this methodology, the detection window can be chosen according to absorption onset of the junction materials. In recent years, the rise of NFAs resulted in quick development of molecules such as ITIC derivatives, followed by the Y6 family. The absorption spectra of NFAs have the great advantage, compared to those of fullerenes, to extend towards the red even near infrared and to be complementary to those of the polymer donors. Although very recent research has shown the realization of red narrow band OPDs based on NFAs, the potential of the application of NFAs to boost the OPD performance remains still largely unexplored.[19,22-24] BHJs based on the mixture between poly[(2,6-(4,8-bis(5-(2-ethylhexyl-3-fluoro)thiophen-2-yl)-benzo[1,2-b:4,5-b']dithiophene))-alt-(5,5-(1',3'-di-2-thienyl-5',7'-bis(2-ethylhexyl)benzo[1',2'-c:4',5'-c']dithiophene-4,8-dione)] (PM6) as donor polymer and 3,9-bis(2-methylene-((3-(1,1-dicyanomethylene)-6,7-difluoro)-indanone))-5,5,11,11-tetrakis(4-hexylphenyl)-dithieno[2,3-d:2',3'-d']-s-indaceno[1,2-b:5,6-b']dithiophene (ITIC-4F) as electron acceptor have demonstrated their great interest in OPVs with high power conversion efficiency (>15%) and good solubility in non-chlorinated solvents which makes them suitable candidates also for OPDs.[25-27] A recent study reported BHJ structures based on 90 nm thick PM6:ITIC-4F films. However, such thin films delivered broadband photoresponse.[28] To the best of our knowledge, no wavelength-selective photodetectors have been achieved with PM6:ITIC-4F BHJ as photo-active layers.

In this work, we report on our systematic study to develop effective NFA-based filter-free visible-blind near-infrared organic photodetectors. Band-selective OPDs have a heterostructure photoactive layer architecture, comprising a PM6:ITIC-4F based-BHJ layer with an extended absorption to longer wavelengths. Based on ultra-thick BHJ layers (> 2 μm), OPDs operating both in normal and inverted structures have been obtained. As a function of thermal annealing temperature, a distinct light response was observed due to molecular rearrangement and a marked misbalance in charge carrier transport. While normal structures switch from narrowband to broadband under thermal annealing, inverted structures improve their spectral fine-tuning over a bandwidth of 42-44 nm to be highly selective at ~806 nm. We demonstrate the first sub-45 nm FWHM visible-blind red photodetectors with a specific detectivity of ~6×10^{12} Jones in an operation mode at 0 V and -2 V reverse bias. The structure and morphology of blend layers have been studied with atomic force microscopy (AFM), contact water angle (CWA) measurement, Raman analyses, and 2D grazing-incidence X-ray diffractometry (2D-GIXRD).

Experimental section

Materials. Patterned ITO substrates (size 25 mm×25 mm) with 15 Ω/sq resistance were purchased from Lumtec, Taiwan. PEDOT:PSS (Al 4083) was purchased from Ossila. For normal structure, ZnO nanoparticle ink was prepared as published previously,[29] while for inverted structure a 2.5 %vol. ZnO nanoparticle solution in alcohol blend diluted to 1 %vol. before use was purchased from Avantama. O-xylene, 1,2,3,4-tetrahydronaphthalene (Tetralin), and molybdenum (VI) oxide (MoO_3 purity 99.97%) were purchased from Sigma-Aldrich. PM6 (Mw~120 kDa; PDI 3.0) and ITIC-4F were purchased from 1-Material. Aluminum (Al) and silver (Ag) were purchased from Kurt J. Lesker. All commercial materials were used as received without purification and kept under nitrogen atmosphere.

OPDs Fabrication. The photodetectors were fabricated in both normal (ITO/PEDOT:PSS/PM6:ITIC-4F/ZnO/Al) and inverted (ITO/ZnO/PM6:ITIC-4F/MoO_3/Ag) structures on ITO-coated glasses using spin-coating technique in glove box under nitrogen atmosphere. First, the ITO substrates were thoroughly cleaned with clean cloth dampened with isopropanol before sonication in isopropanol for 30 min and applying UV ozone for 15 min at 80°C. For normal architecture, a thin layer of PEDOT:PSS with thickness of 40 nm was spin-coated on cleaned ITO substrates at 3500 rpm for 60 sec, followed by an annealing step at 120°C for 15 min. Different blend solutions of PM6:ITIC-4F (38 mg/mL and 51 mg/mL for ratios 1:1 and 1:2, respectively) for the photoactive layer were used in (95% volume) o-xylene and (5% volume) Tetralin. Inks have been stirred at 50°C overnight. PM6:ITIC-4F layers were spin-coated inside nitrogen-filled glove box at 500 rpm for 120 s following by a post-deposition thermal annealing at different temperatures (100°C, 150°C or 200°C for 10 min). To complete devices, 30 nm of ZnO was spin-coated at 2000 rpm for 60 s before annealing at 100°C for 180 s and Al was thermally evaporated to an electrode thickness of 100 nm under a vacuum of 2×10^{-6} mbar through a shadow mask to obtain device areas of 0.09 and 0.25 cm^2. For inverted architecture, a thin layer of ZnO was spin-coated on the cleaned ITO substrate in the ambient conditions at a speed of 5000 rpm for 60 s followed by an annealing step inside nitrogen-filled glove box at 100°C for 10 min to form 15 nm thick film. The active layer based on PM6:ITIC-4F was deposited from inks at 40 mg/mL and 60 mg/mL for ratios 1:1 and 1:2, respectively in (95%

volume) o-xylene and (5% volume) Tetralin. Inks have been stirred at 50°C overnight. MoO_3 and Ag were successively thermally evaporated at 2×10^{-6} mbar to 2 nm and 100 nm thick layers respectively using the same shadow mask as for normal structure devices.

***OPDs characterization*.** The dark current density-voltage (J-V) characteristics of the devices were measured in a light occulting Faraday cage inside the glove box using a Keithley 238 Source Measure Unit allowing to measure tens of femtoamperes. One-meter triax leads were used to minimize the measurement noise. The same setup was used for light J-V measurements with devices out from Faraday cage to be exposed to a Newport solar simulator (Sol3A Class AAA, IEC/JIS/ASTM, 450 W Xenon, 4×4 in. Model: 94043A) with an irradiation intensity of 100 mW cm^{-2}. The light intensity was determined with a Si reference cell (Newport Company 2×2 cm calibrated solar cell made of monocrystalline silicon and a fused silica window Model: 91150V) calibrated by the National Renewable Energy Laboratory (NREL). EQE measurements were processed in a dark room in ambient conditions with a 150 W Xe arc lamp Apex illuminator (70525) light source collimated to a Cornerstone™ 260 1/4m UV-VIS Monochromator (74125) from Oriel Instruments for the light part and with a Keithley 238 Source Measure Unit for the electrical part. Devices were mounted on an optical table in a Faraday cage with an aperture to expose the samples to the monochromatic light. The electrodes of the devices were electrically connected to the cage by spring loaded pogo pin connectors. The light beam was filtrated with 295 nm (10CGA-295) and 570 nm (10CGA-570) longpass filters before reaching the devices. Light Dependent Resistor (LDR) measurements were processed with an OSLON®Black 4 PowerStar IR (ILH-IO04-81SL-SC211-WIR200) which is a 4 LEDs network SMD from Intelligent Led Solutions as high light intensity source placed in front of mounted devices together in a Faraday cage, with LED current controlled with power supply and OPD current measured with Keithley 238 Source Measure Unit. For LDR measurement, the thicknesses of films were measured to be 1.34 µm and 1.18 µm for 1:1 and 1:2 w/w ratio, respectively.

The responsivity $\Re$ is calculated from the EQE spectra, using the following equation:

$$\Re = \frac{J_{ph}-J_d}{L_{opt(\lambda)}} \approx \frac{J_{ph}}{L_{opt(\lambda)}} = EQE.\frac{\lambda q}{hc} \qquad \text{(eq. 1)}$$

where J_{ph} is the current density under illumination, in $mA.cm^{-2}$, L_{opt} is the incident light power density, in $mW.cm^{-2}$. J_d is the dark current density and is extremely small as compared to J_{ph} and therefore can be neglected.[30]

***Fabrication and measurements of Space Charge Limited Current devices*.** Space Charge Limited Current (SCLC) devices require careful choice of the contacts to ensure sufficient injection of the desired carrier, and effective blocking of the other carrier to work like single-carrier devices.[31] Hole-only and electron-only devices consisted of ITO/PEDOT:PSS/PM6:ITIC-4F/MoO_3/Au and ITO/ZnO/PM6:ITIC-4F/LiF/Al, respectively. In SCLC based devices, the mobility is measured vertically in the entire bulk of the active layer sandwiched between the two interfacial layers. Top metallic electrodes were thermally evaporated (MBRAUN evaporator inside the glovebox) at 2×10^{-6} mbar to a controlled thickness (13 nm of MoO_3, 100 nm Au, 0.5 nm LiF and 100 nm of Al) using a shadow mask that defines the device areas to 0.09 cm^2 or 0.25 cm^2 and allows a four-probes measurement. SCLC four-probes measurements were done in the same Faraday cage as for OPDs inside the glovebox. The pristine PM6:ITIC-4F (1:1 or 1:2 ratio, at concentration of 20 mg/mL and 30 mg/mL respectively) solutions were deposited by spin-coating at 1000 rpm for 60 sec. Active layers were subsequently annealed at 100°C, 150°C or 200°C during 10 minutes. The thicknesses of films were measured precisely with a DEKTAK XT profilometer from Bruker.

The measured dark current was fitted using the Murgatroyd expression:

$$I = A\mu_0 \frac{9}{8}\frac{V^2}{d^3}\varepsilon\varepsilon_0 \exp\left(0.891\gamma\sqrt{\frac{V}{d}}\right) \qquad \text{(eq. 2)}$$

where d is the active layer thickness, A is the active device area, $\varepsilon\varepsilon_0$ is the permittivity of the active layer (ε is assumed equal to 3.5 and ε_0 is the permittivity of free space), and V is the voltage. μ_0 and γ are the unknown parameters that will be adjusted to get a good fit, all other parameters are fixed. μ_0 is the mobility at low electric fields, and γ is a parameter that represents the field dependence of mobility.

Characterization of Organic films. The absorbance of the active layer films was measured by UV–Vis–near infrared Spectrophotometer Cary 5000. The surface morphology of the blend layers was investigated by AFM (NTEGRA from NT-MIDT) in semi-contact mode using the

silicon tips (MikroMash) with a theoretical resonant frequency of 150 kHz and a force constant of 5.4 $N.m^{-1}$ at room temperature. Film thicknesses were measured by a stylus profilometer (Bruker DEKTAK XT) with 1 mg force on the probing tip. Contact water angle (CWA) measurements were performed with an optical contact angle (OCA) series 15EC with high resolution USB camera and sample positioning from DataPhysics Instrument GmbH Company in a room with a controlled temperature at 20ºC.

Thin films were further analyzed with high-brightness synchrotron radiation at BL19B2 in SPring-8 (Japan). GIWAXS (Grazing-Incidence Wide-Angle X-ray Scattering) measurements were performed using a high-sensitive 2D X-ray detector (PILATUS 300K). The incident angle and wavelength of X-rays were 0.13° and 0.100 nm, respectively. The crystal coherence length (CCL) values were extracted by the Scherrer equation:

$$\tau = \frac{K\lambda}{\beta \cos\theta} \qquad \text{(eq. 3)}$$

where τ is the ordered (crystalline) domains mean size, here defined as CCL, K is a constant (dimensionless shape factor) closed to unity. The shape factor is typically equal to 0.9, λ is the wavelength of the X-ray, β is the FWHM of the diffraction peak in radians after subtracting the instrumental line broadening and θ is the Bragg angle.

For Raman spectroscopy measurements, neat (PM6 and ITIC-4F) and PM6:ITIC-4F BHJ layers are deposited on ZnO buffer layers. The technique uses a source of monochromatic light, usually from a laser in the visible, near infrared, or near ultraviolet. The laser light interacts with molecular vibrations, phonons or other excitations in the system, resulting in the energy of the laser photons being shifted up or down. Raman microprobe measurements were done using a HR800-UV Horiba-Jobin Yvon spectrometer coupled with an Olympus metallographic microscope. The measured spectra were obtained using as excitation the red line of He-Ne laser (λ = 632.8 nm). Raman spectrometer calibration was performed before every Raman experience with a monocrystalline Silicon wafer. The Si-Si vibration mode at 520.7 cm^{-1} was used as reference.

RESULTS AND DISCUSSION

1. OPDs spectral responses

The chemical structures of organic compounds and device architectures used in this work are shown in Figure 1a. The normalized ultraviolet-visible (UV-vis) optical absorption spectra of the neat materials and blend thin films (ratio 1:1) are shown in Figures 1b. The as-cast ITIC-4F film exhibits a clear red-shifted absorption with λ_{max} at 724 nm leading to a complementary absorption with the donor polymer (λ_{max} = 617 nm for as-cast film) resulting in a lower optical bandgap ($E_{g,opt}$) for ITIC-4F (1.53 eV) compared to PM6 (1.81 eV). In addition to as-cast films, the absorption of films was measured as a function of post-annealing temperatures (100°C, 150°C and 200°C). While there is no strong change in the absorption spectra of the PM6 polymer suggesting an isotropic arrangement of the polymer chains, a strong red-shift of 41 nm of the low energy band is observed for the neat ITIC-4F film post-annealed at 200°C. Regardless of the post-annealing temperature, the absorption spectra of PM6:ITIC-4F blends correspond to the superposition of the two corresponding films whereby the red-shift is also observed at 200°C with a value of 31 and 35 nm for 1:1 and 1:2 ratio, respectively (see Figure S1 for 1:2 ratio, ESI†). Because of the greater amount of ITIC-4F in the 1:2 ratio, its relative peak is more intense to match that of the polymer. In a very pronounced form, this peak increases especially at 200°C for both ratios, highlighting an increase of the molecular absorbance area due to a rearrangement of the molecules in layers. The red shift and increase of the ITIC-4F peak indicate an increase in thermal-induced aggregation and thus better organization of molecules, where a predominance J-like aggregates in ITIC-4F films have been reported.[32-34]

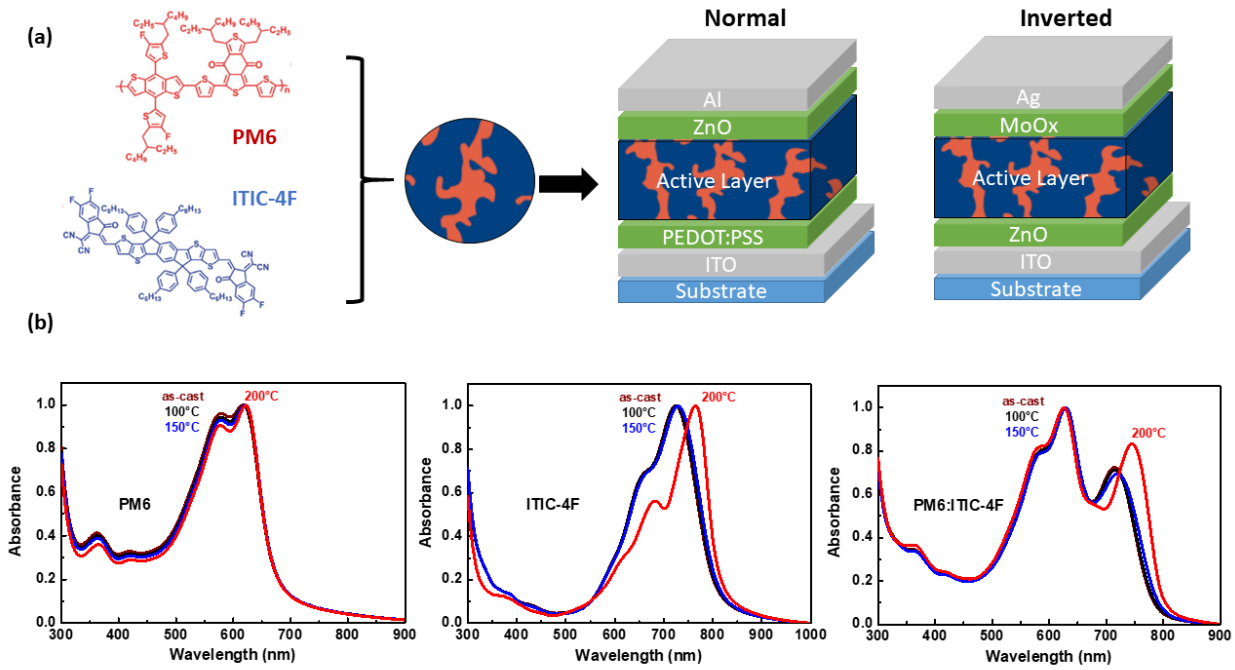

Figure 1. (a) Chemical structures of PM6 and ITIC-4F and schematic multi-layer device structures of organic photodetectors. (b) Normalized UV-Vis absorption spectra of neat and blended films for as-cast and thermal annealed layers at 100°C, 150°C or 200°C.

Based on PM6:ITIC-4F BHJ films, OPD devices are realized in normal and inverted structures. As expected, for the thinnest junction (~200 nm), all incident wavelengths induce bulk carrier generation, with electrons and holes collected efficiently due to the relatively short extraction distance to their respective extraction electrode. The device is considered optically and electrically thin, showing no color discrimination to be effectively broadband (see Figure S2, ESI†).[21] Increasing the junction thickness produces a higher charge generation near the illuminated surface for wavelengths below 750 nm (*i.e.* incident photons with high absorption coefficients) with respect to the charges generated near the opposite electrode. In the limit, the junction with a thickness higher than 2 µm delivers a narrowband response centered at ~800 nm due to a CCN effect (Figure S2, ESI†). Thickness control is therefore a crucial parameter to achieve a narrowband response in OPD. In addition, the morphology of films also holds a key role.[17,19,22,35,36] The molecular arrangement of small molecules but also of polymers and

consequently of blends can be thermally modified.[25,32] Therefore, it is of interest to study the effect of thermal post-annealing temperature on the performance of narrowband OPDs.

Figure 2a and S3a (see ESI†) show EQE spectra at zero bias (0 V) of PD-type OPDs based on BHJs in 1:1 ratio post-annealed from 100°C to 200°C with inverted and normal structures, respectively. The OPDs were fabricated with micrometric ultra-thick PM6:ITIC-4F (see Table S1 for precise thicknesses, ESI†). At 100°C, the results demonstrate that our OPDs exhibit a low contribution to the photocurrent from visible wavelengths together with narrow peaks of 11% at 782 nm and 11.6% at 802 nm for inverted and normal structure, respectively (Table S1, ESI†). The narrowband response of these PD-type OPDs follow the CCN concept proposed by Meredith *et al.*.[19] Depending on the structure, EQE spectra shows opposite trends under thermal annealing. As shown in Figure 2a, the visible-blind property (300-750 nm) is accentuated from 100°C to 200°C for inverted together with a maintained spectral selectivity around 780-800 nm. On the contrary and despite an increase of the CCN peak, the normal structure loses its selectivity by applying higher annealing temperatures (Figure S3, ESI†). This loss is mainly characterized by the occurrence of a broad band detection between 300 and 500 nm. By applying a negative bias at -2 V to inverted and normal PD-OPDs, EQE spectra show the same trends as a function of temperature, but with higher values throughout the spectral range (Figure 2b and S3 in ESI†). Such phenomenon is commonly attributed to the enhanced collection of photogenerated charge carriers at large biases.[23,36,37] From EQE measurements, calculated responsivity ($\Re$) spectra using the equation (1) were plotted to determine the maximum value centered on the CCN peak. Figure S4 (ESI†) shows the calculated $\Re$ spectra of OPDs in inverted structure under 0 V and -2 V biases. The responsivity $\Re$ reaches a maximum value of 159.6 $mA.W^{-1}$ at -2V for OPDs based on 1:1 ratio at 200°C. A spectral rejection ratio (SRR) is calculated as $\Re$ ratio of highest value to that at 460 nm. Table S1 (ESI†) summarizes the OPD parameters of devices in normal and inverted structures. A maximum SRR of 80.5 is obtained for inverted OPDs based on 1:1 ratio at 200°C with a FWHM of 42 nm at -2 V. On the contrary, the SRR decreased to 1.8 at 200°C for normal OPDs, confirming that OPDs lost their selective detection capability at high thermal annealing temperature to no longer be identified as CCN OPDs. The FWHM of CCN peak is only marginally affected with a value < 45 nm regardless of the temperature. We demonstrate the first sub-45 nm FWHM visible-blind red photodetectors, half that of a planar heterojunction (PHJ) structure based on PM6 and ITIC-4F.[38] Moreover, in

both structures, the shift to longer wavelength of the CCN peak is consistent with the shift of the onset of the absorption peak.

By doubling the amount of ITIC-4F to achieve a 1:2 ratio, inverted OPDs show a CCN peak only at the highest thermal annealing of 200°C centered at 818 nm (Figure S5, ESI†). Despite a higher EQE value of 10% versus 8.45% for the 1:1 ratio at 0 V, SRR decreases by half to 38.1 (Table S1, ESI†). This trend, characterized by a small increase of CCN peak and a high decrease of SRR, is commonly observed for the 1:2 ratio independently of structure, annealing temperature and applied bias (Figures S3c, S3d and S5, ESI†). As previously reported, ITIC-4F molecules are efficiently blended in the volume formed by the polymer chains, and hence contributes to both surface and volume photons absorption and carriers generation.[27] The amount of collected carriers increases accordingly, which strengthens the CCN peak but also weakens the blinding property in the visible range. With lower SRR values, the addition in excess of ITIC-4F is not favorable to obtain selective PM6:ITIC-4F based PD-OPDs.

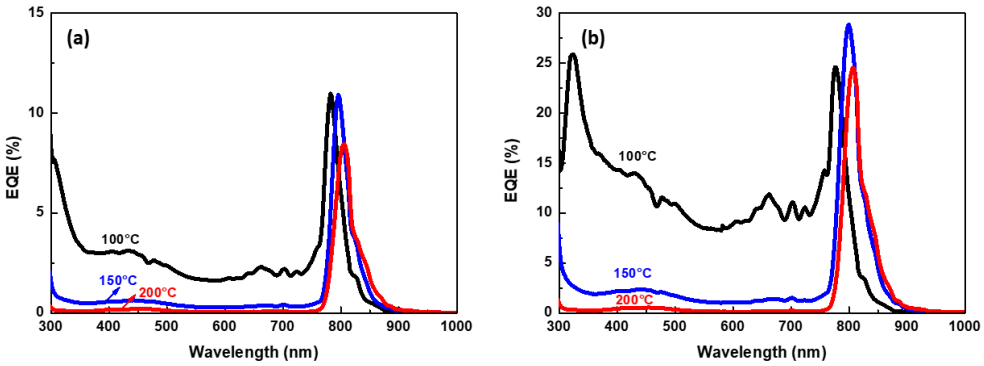

Figure 2. External quantum efficiency (EQE) spectra of photodiode devices in inverted structure as ITO/ZnO/PM6:ITIC-4F(1:1 w/w ratio)/MoO_3/Ag and by varying the thermal annealing temperature of the active layers from 100°C to 200°C under different biases (a) 0 V and -2 V (b).

2. Surface analysis of PM6:ITIC-4F blends

The surface topography of PM6:ITIC-4F blend films deposited on ZnO-modified ITO substrates was first characterized by AFM. Figure 3 (and Figure S6 at larger scale, ESI†) compares the

AFM images of thermally annealed PM6:ITIC-4F BHJs at 100°C, 150°C and 200°C. Importantly due to their high decomposition temperatures (300°C for ITIC-4F and 420°C for PM6), we can consider that the studied films exhibited great thermal stability and are not degraded at a thermal post-annealing temperature up to 200°C.[39-43] Regardless of the ratio, BHJ layers at 100°C and 150°C have the same small roughness of 2-4 nm and very similar fibril structures, while 200°C films show larger angular-shaped aggregates and an increased roughness to a maximum of 21.8 nm. Such aggregates have well-defined edges at the intersection of roughly planar faces. According to the AFM images of neat PM6 shown in Figure S7 (see ESI†), the morphology of PM6 shows no modification under post-annealing. On the contrary, thermal treatment should increase the aggregation of small molecules such as ITIC-4F in blend and thus change the morphological properties of the layers. Figure S8 provides evidence of this, but in the case of the neat ITIC-4F film, the molecules form layers composed of large and densely packed round-shaped aggregates at 200°C with a roughness almost 5 times higher than at 100°C with a value of 1.96 nm. Although we can attribute the aggregation of the blend to the aggregation of ITIC-4F at high temperature, the high post-annealing temperature greatly affects the shape of aggregates and the roughness value. The resulting surface morphology will necessarily lead to strong differences in the surface wettability.

To provide information on the evolution of the surface wettability of the blend, we realized WCA characterization on thermally annealed blends (Table S2 and Figure S9, ESI†). The WCAs of pure PM6 and ITIC-4F films were also performed as references. Both ITIC-4F and PM6 surfaces are hydrophobic with average WCA above 90 . However, with the lowest WCA, ITIC-4F films are less hydrophobic compared to PM6 films independently of thermal temperature. At 100°C, blend layers delivered a comparable WCA value to the neat PM6 layer with values of 101-103°. By increasing the temperature, WCA values increase to reach 107-108°where a demixing of ITIC-4F when blended with PM6 could be thermodynamically favourable as reported by Brabec *et al*.[25] However, with higher values than those of neat films, this significant increase cannot be ascribed to the appearance of one material rather than another on the top surface but is subsequent to the very large increase in roughness value at 200°C. The WCA depends on (i) the surface chemistry upon the presence of polar or nonpolar moieties on the surface, which regulates the type of interactions, either attractive at the solid/liquid interfaces or repulsive but also on (ii) topographic structures revealed by the surface roughness.[44] As

described by Wenzel's model,[45] roughness can enhance both the hydrophobicity and hydrophilicity in the sense that the roughness makes a hydrophobic surface more hydrophobic, or more hydrophilic if the surface is originally hydrophilic. We can therefore assign here that the hydrophobicity of blends at 200°C is directly related to the morphology of their rough upper surfaces.

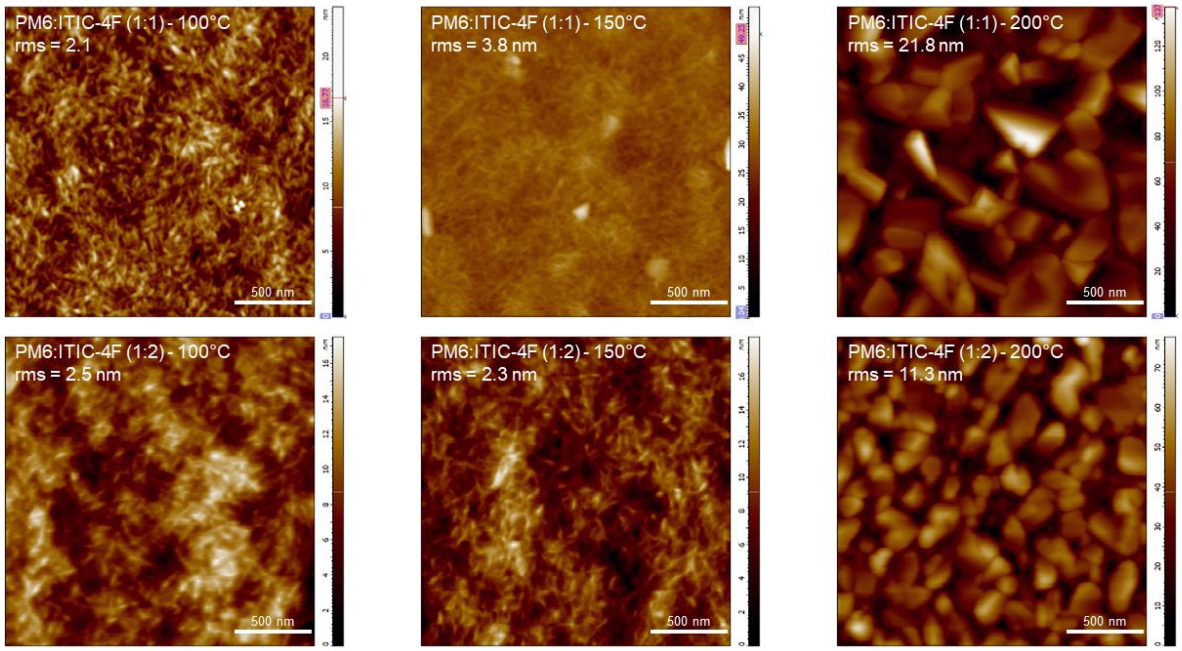

Figure 3. Atomic force microscopy height images of PM6:ITIC-4F bulk heterojunction blends (1:1 ratio on top and 1:2 ratio on bottom) post-annealed at 100°C, 150°C and 200°C. Scale: 2×2 μm^2.

3. Bulk analysis of PM6:ITIC-4F blend films

AFM and WCA, as surface analysis techniques, will not reveal whether thermal annealing induces molecular reorganization in volume. It is therefore necessary to use other analytical techniques to probe the volume structural state of the blends. For further analysis of the thermal-induced aggregation in blend films, GIWAXS analysis were performed. In GIWAXS, a very shallow incident angle is applied allowing the beam to travel a long path inside the organic film before the data are collected in reflection. For this reason, X-ray scattering techniques are

extensively used to study inner morphology.[46] We compare 2D diffraction patterns (q_{xy}, q_z) and the corresponding in-plane (IP) and out-of-plane (OOP) intensity profiles of annealed BHJ layers (in 1:1 and 1:2 ratios) as function of thermal annealing temperature. From Figure 4 and Figure S10 (in ESI†), we see that in all cases thermal annealing enhances strongly the crystallinity of the films expressed by much brighter and sharper scattering peaks. The Gaussian fit of the (100) OOP peaks for the three temperatures reveals that there are two populations of crystalline organization in the blend. In order to assign each peak to either PM6 or ITIC-4F, neat materials were analyzed as references. At 100°C, PM6 films are composed of highly ordered crystallites as noted by an intense and narrow diffraction peak indexed (100) at q_z = 0.327 $Å^{-1}$ in OOP profile (Figure S11 and Table S3, ESI†). It is attributed to the edge-on lamellar stacking of PM6 with a lattice constant (*d*-spacing) of 1.92 nm and a CCL of 1.10 nm. By increasing the temperature to 200°C, PM6 films do not show a significant increase in crystallinity with the (100) peak at q_z = 0.325 $Å^{-1}$ in OOP profile, a *d*-spacing of 1.93 nm and a CCL of 1.58 nm. According to this predominant edge-on molecular orientation of PM6 chains with respect to the substrate, the IP profiles show a weak (010) peak at 1.73 $Å^{-1}$ corresponding to a π–π stacking with a *d*-spacing of 3.63 nm.[25] For neat ITIC-4F layers, a poor self-organization behavior has been observed at low thermal annealing temperature to reach a preferential lamellar stacking in both edge-on ((100) peak at q_z = 0.446 $Å^{-1}$ in OOP profile) and titled edge-on molecular plane orientation in films annealed at 200°C.[32]

The profile of neat materials helps us to assign each peak to either PM6 or ITIC-4F. Table S3 (see ESI†) provide the XRD data obtained from the experiments and the Gaussian fit. One peak at q_z around 0.31-0.33 $Å^{-1}$ is assigned to PM6, while the second at q_z = 0.4-0.41 $Å^{-1}$ corresponds to ITIC-4F. For PM6, we can observe a shift of (100) peak in OOP with the temperature. This results in an increase of *d*-spacing of PM6 polymer chains from 1.84 to 1.97 nm for 100°C to 200°C. For ITIC-4F small molecules, *d*-spacing remains constant with a value of 1.50-1.55 nm. The CCL obtained by the Scherrer equation (eq. 3) is not greatly influenced by temperature, with consistently higher values for ITIC-4F than for PM6. There is therefore no significant phase segregation under thermal annealing. More importantly, the Gaussian fit highlights an increase in the contribution of ITIC-4F to the total peak area with temperature suggesting specific blend-induced crystallization with an edge-on lamellar packing of ITIC-4F molecules in high temperature annealed blends. By changing the buffer layer to PEDOT:PSS involved in normal

structure, the same tendencies have been observed (Figure S12 and Tables S3, ESI†). Nevertheless, and in contrast to neat ITIC-4F films, the typical diffraction peak (100) is as intense and narrow in the IP as in the OOP profiles, implying that a face-on lamellar orientation of ITIC-4F crystallites is also induced in blends at 200°C. More surprisingly and by the volume integration of ITIC-4F molecules in PM6 polymer chains, an induced face-on orientation of PM6 is also highlighted by the emergence of the (100) peak in IP. The face-on orientation of crystallites at 200°C is also highlighted by an intense (010) diffraction peak in the OOP direction corresponding to the π–π stacking. With a more refined analysis of this peak (Figure S13, ESI†), we can observe sub-structures at 1.734 $Å^{-1}$ corresponding to the (010) peak of PM6 and at 1.83 $Å^{-1}$ to ITIC-4F with a *d*-spacing of 3.45 nm.[39] This second majority peak can only be assigned to the π-π stacking of ITIC-4F as its contribution increase in 1:2 ratio (Figure S13b, ESI†).

Diffraction patterns provide specific information about the microstructure of each material in blends. ITIC-4F small molecules are subjected to a specific blend-induced crystallization with a bimodal lamellar stacking on both edge-on and face-on orientation in high temperature annealed blends. These changes will have a direct impact on PM6 polymer chains which will no longer be organized exclusively edge-on, but also according to a face-on orientation. A simultaneous face-on orientation of both materials is induced in BHJs.[47] Such bimodal orientation can only be favorable for 3D-charge carrier transport allowing a vertical transport with respect to the substrate, corresponding to the direction involved in the sandwich structure of OPDs.

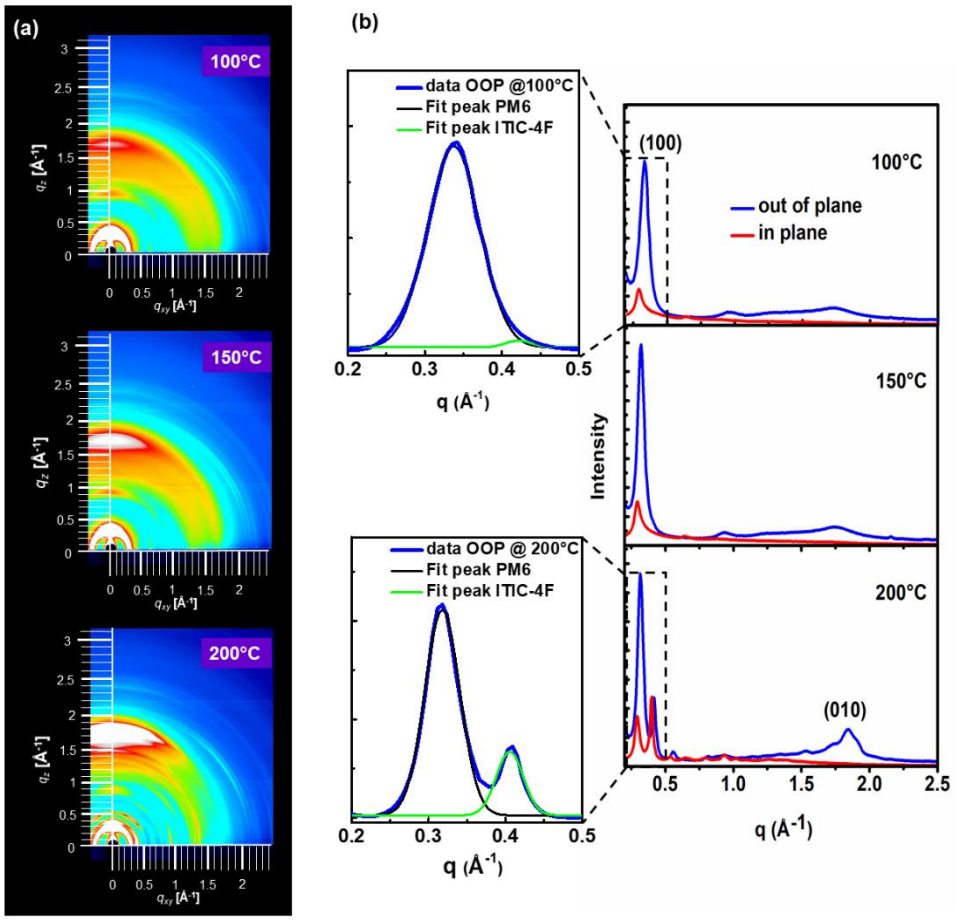

Figure 4: 2D-GIXRD patterns (a) and corresponding in plane (IP) and out of plane profiles (OOP) (b) of PM6:ITIC-4F (1:1 w/w ratio) blend layers deposited on ZnO buffer layer as function of thermal annealing temperature. Zoom with Gaussian fit of (100) OOP peaks.

Even though GIWAXS probes the whole layer in volume, different molecular morphologies can occur between the bottom and the top of the layer. In the present study, we therefore performed Raman measurements on both sides of the ultra-thick layers (front side on the top surface layer and back side through the transparent substrate). For this, we coupled a long working distance objective (Olympus SLMPN5X, WD 18 mm) to access the back of the layer through the glass substrate. The same objective was used on the other surface to collect both spectra on the same conditions. Raman can probe molecular conformation as well as chemical structure as it is sensitive to the polarizable electron density, e.g. π-conjugated systems, providing important information about structural and morphological changes in semi-crystalline materials.[48] Raman spectra from the front side of ultra-thick PM6:ITIC-4F blend as a function of annealing

temperature are presented in Figure 5. Raman peaks appear better defined at 200°C as was expected but, regardless of the annealing temperature, well-structured spectra with several Raman peaks are observed in all the samples, suggesting the formation of a crystal order in blend even for the lowest temperature of annealing. To assign the different peaks in the blend spectra to PM6 or ITIC-4F, Figures S14a and b (see ESI†) show Raman spectra of neat PM6 and ITIC-4F layers at 200°C. At this temperature, both PM6 and ITIC-4F neat films exhibit high crystalline structures allowing to identify their respective peaks. Crystalline ITIC-4F films specifically present the signals of the C-C intra-ring stretching mode at 1248 cm^{-1} and the fused phenyl ring at 1600 cm^{-1}.[33] Peaks at 970 cm^{-1}, 1138 cm^{-1}, 1340 cm^{-1} and 1600 cm^{-1} are clearly assigned to ITIC-4F, while the peaks at 1075 cm^{-1} and 1230 cm^{-1} can be addressed to the PM6 polymer alone. Finally, peaks appearing in the region from 1400-1550 cm^{-1} are a contribution from both materials. Figure S14c (see ESI†) shows the Raman spectra of the back side. The same assignment of the peaks can be applied in Figure 5 and in Figure S14c, revealing a similar structure regardless of the face suggesting a bi-continuous interpenetrating network in thick films. In both cases, specific peaks assigned to ITIC-4F are more pronounced at 200°C. This result correlates well with GIWAXS data that indicate induced crystal order in the blend layers.

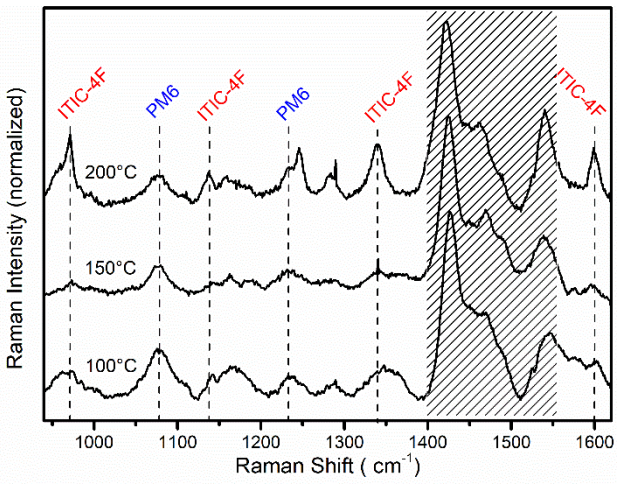

Figure 5: Raman spectra from the front side of ultra-thick PM6:ITIC-4F blends with 1:1 w/w ratio post-annealed at 100°C, 150°C and 200°C.

4. Transport and collection of charge carriers

In narrowband OPDs, EQE spectra strongly depend on photon harvesting, exciton dissociation, charge carrier transport and collection. Due to a mixture of PM6 and ITIC-4F in a bi-continuous interpenetration network in the entire volume as well as a complementary absorption range, we can assume that harvesting of photons and exciton dissociation are as efficient at the surface as in the volume of the layer. In order to understand why EQE evolved under thermal annealing, one of the parameters to be examined is the mobility of both holes and electron. The charge transport properties of the blend films were determined as function of PM6:ITIC-4F weight ratio (1:1 and 1:2) and thermal annealing temperature (100°C, 150°C and 200°C). To this end, we used the SCLC protocol described by Blakesley *et al* to extract the mobility from I-V curves of hole-only devices and electron-only devices.[49] I-V curves were fitted using equation (2) in the SCLC region considering a field-dependence of the mobility (Figure S15, ESI†). Hole (μ_h) and electron (μ_e) mobility values obtained for PM6:ITIC-4F BHJ layers together with the values of thicknesses are summarized in Table S4 (see ESI†). Figure 6 shows representative evolution of hole and electron mobility values for hole and electron only devices with thin layers (thickness range of 146-243 nm). Based on hole-only devices, the hole mobility dropped with thermal annealing from 2.46×10^{-4} cm^2/Vs at 100°C to 1.79×10^{-6} cm^2/Vs at 200°C for 1:1 ratio. For 1:2, this decrease is even more accentuated due to a lower proportion of polymer chains compared to ITIC-4F molecules that obstruct the percolation paths of the holes. Less efficient hole transport can be explained by the formation of less dense polymer crystallites where an increase of *d*-spacing from 1.84 to 1.97 nm at 100°C and 200°C was observed in blends by GIWAXS, respectively. In contrast, the electron mobility increases proportionally with the temperature. The electron mobility reaches the maximum average value of 3.68×10^{-4} cm^2/Vs and 6.71×10^{-4} cm^2/Vs for 1:1 and 1:2 ratio at 200°C, respectively. These mobility values are in accordance with to those obtained by Brabec *et al.* for post-deposition thermal annealed PM6:ITIC-4F blend systems.[25] In each ratio, while the hole mobility is greatly reduced, the electron mobility increases by one order of magnitude from 100°C to 200°C to be the fastest charge carriers. Consequently, a high imbalance between electron and hole mobility values is measured with $\mu_e/\mu_h = 205$ at 200°C vs. $\mu_e/\mu_h = 0.13$ at 100°C and $\mu_e/\mu_h = 3388$ at 200°C vs. $\mu_e/\mu_h = 39$ at 100°C for 1:1 and 1:2 ratios, respectively. Although electron mobility could not be measured at 100°C for 1:1 ratio, an equally high electron mobility (5.9×10^{-4} cm^2/Vs) together with a μ_e/μ_h ratio at

200°C of 145 have been measured for thicker layers (thickness > 1800 nm). These results highlight the great facility of electrons to be mobile into the bi-continuous thick network post-annealed at 200°C. Accordingly, blend-induced crystallization with a face-on orientation of ITIC-4F small molecules observed by GIWAXS generates a very efficient vertical electron transport with respect to the electrodes in thermally annealed films at 200°C.

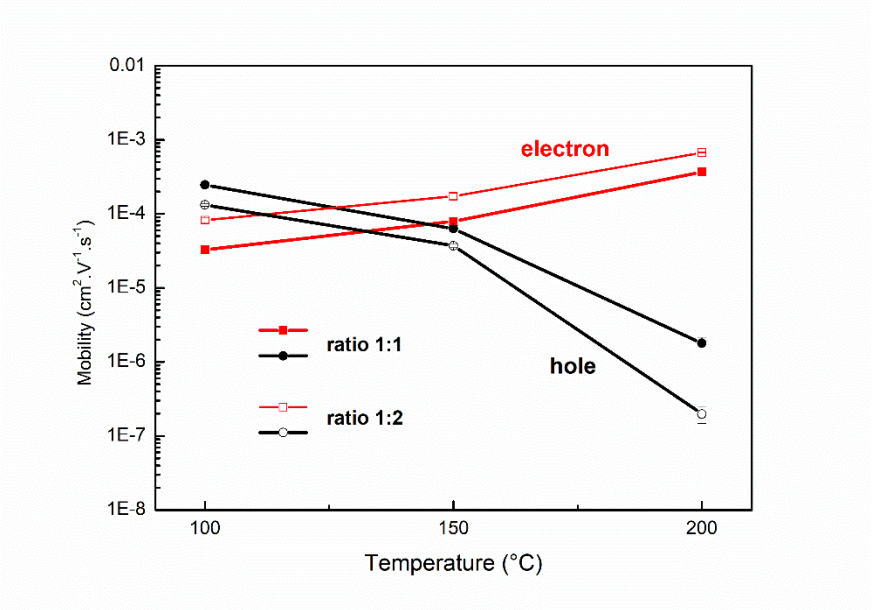

Figure 6: Evolution of hole and electron mobility values as function of thermal annealing temperature of PM6:ITIC-4F blends (1:1 and 1:2 w/w ratio). Hole and electron only devices with a thickness between 146 and 243 nm.

We can describe PM6:ITIC-4F blends as bi-continuous interpenetrating networks. Consequently, as do the thinner layers, thick BHJs can be modelled as a single effective medium.[28] However, for thin BHJs, charge carrier distribution across the active layer at 1 sun is relatively homogeneous, which is no longer the case for thick films. With layers of micrometric thickness greater than 2 µm, our ultra-thick PD-type OPDs are described as being optically and electrically thick.[21] The outcome and, consequently, specifically the collection of these charges at their respective collection electrode will therefore contribute or note to the EQE spectra. To investigate the evolution of spectra as a function of active layer thickness, Figure S16 (see ESI†) shows EQE spectra at zero bias (0 V) of inverted PD-type OPDs based on BHJs in 1:1 ratio post-annealed at 100°C and 200°C with an active layer thickness ranging from 225 to 1345 nm. At comparable thickness, EQE spectra show different spectral responses at 200°C and 100°C. For

thinner layers, while broadband EQE are collected, the selective peak in progress at ~800 nm is already pronounced at 200°C. By increasing the thickness, this single peak predominates at 200°C to deliver a narrow wavelength-selective photodetection, which will never be reached at 100°C even with ultra-thick layers (> 2 µm) as observed in Figure 2a. It is therefore obvious that there is a joint correlation between the induced increased crystallinity of the ITIC-4F domains and changes in charge carrier mobility at 200°C.

To illustrate the operating principle of our OPDs, schematic images were drawn to describe the distribution and transport of charges generated by different wavelengths in the ultra-thick PM6:ITIC-4F active layers (Figure 7). Distinctions have been made according to the wavelength of illumination through the transparent ITO electrode, *i.e.* λ_{BL} correspond to visible photons (300 nm < λ_{BL} < 750 nm) and λ_{CCN} correspond to red photons from the tail of the absorption band (λ_{CCN} > 750 nm). It is important to notice that spectral ranges of these two wavelength domains correspond specifically in the present study to absorption PM6:ITIC-4F active layers (see Figure 1b). From the optical point of view, visible photons coming from λ_{BL} are mostly absorbed near the transparent (light input side) electrode with a Beer-Lambert-like profile to generate surface charges, while red photons from λ_{CCN} can penetrate into the volume resulting in the generation of both surface and volume charges. Since the core of the CCN effect is based on the collection of these photo-generated charge carriers, the outcome of these charges is of primary importance. As specified by Armin *et al.*, the basic CCN mechanism originates from the recombination of surface-generated charges either geminately or non-geminately.[19] The attribution of electrically thick refers to layers that give rise to charge carrier recombination and poor charge collection of carriers generated near the illuminated transparent electrode under λ_{BL}. Only the charges generated in the red under λ_{CCN} will produce charge carriers that will be efficiently extracted to create the CCN spectral peak in the EQE. This is in agreement with the EQE spectra measured at 100°C for both normal and inverted architectures (Figures 2 and S3, ESI†).

The next question to address is why one structure strengthens its CCN character while the other loses it under thermal annealing. The two structures can be described by an electrical inversion such that the transparent illuminated electrode is extracting holes (anode) in normal and electrons (cathode) in inverse. Consider first the case of the normal architecture, electrons derived from λ_{BL} photons are generated near the anode and by consequence, much further away from their extracted electrode (the cathode). These electrons must travel across the active layer thickness.

At 100°C electrons have lower mobility compared to holes, resulting in a low extraction rate due to a transit time (time for free electrons generated at a given position to reach their extraction electrode) longer than their life time τ_e. This results in a higher electron density near the ITO/PEDOT:PSS contact, which reduces the hole lifetime, to participate in a very strong recombination near the transparent hole-extracting contact (Figure 7a). Therefore, there is almost no response in the λ_{BL} wavelength range. Only electrons generated in volume by red photons (λ_{CCN} photons) are collected and give a narrow CCN peak (Figure 7b). At 200°C, the electron mobility is highly increased which will decrease their transit time to be shorter than τ_e. The electrons drift length ($L_{D/e}$) will be extended to their extraction electrode through the blend layer, allowing efficient charge collection even under λ_{BL}, as shown in Figure 7a. Electrons generated deeper in volume relative to their extraction electrode will be collected and participate in an EQE response in both spectral ranges λ_{BL} and λ_{CCN}, eliminating the blinding property of the OPD and enhancing the CCN peak, respectively (see EQE spectra at 200°C in Figure S3, ESI†).

In inverted architecture, these are the holes that must now pass through the thickness of the active layer. At 200°C, holes have a much lower mobility, which results in a longer transit time, a resulting increased concentration of holes near the transparent cathode will appear under λ_{BL} (Figure 7c). The drift length of the holes ($L_{D/h}$) will be too short to allow extraction. This results in a recombination of the charges generated near the cathode and thus a more important blinding phenomenon in the visible range compare to 100°C. Under λ_{CCN} (Figure 7d), with a highly increased mobility of the electrons at 200°C and their favorable percolation paths, the quantitative number of electrons that will be collected to participate in the CCN peak will increase regardless of layer thickness as observed on Figure S16.

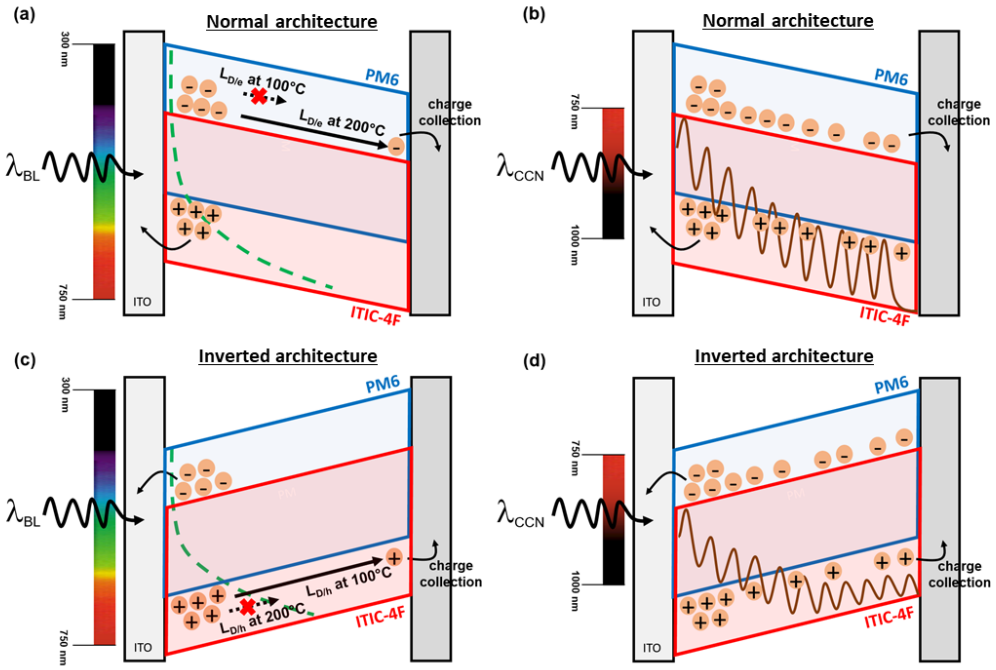

Figure 7: Schematic representation of the operating principle of ultra-thick OPDs based on PM6:ITIC-4F blends.

5. Performance metrics of the PD-OPDs

Having established the basic principles for making an effective narrowband NFA-based filter-free visible-blind near-infrared OPDs, we now proceed to the characterization of their light detection properties. The optimized OPDs with the highest SRR value are obtained in inverted structures with a PM6:ITIC-4F blend in weight ratio of 1:1 and 1:2 with an annealing process at 200°C. The corresponding calculated responsivity ($\Re$) spectra in Figure S4 delivered a maximum value of 159.6 mA.W^{-1} and 126.2 mA.W^{-1} at -2V for 1:1 and 1:2 ratio, respectively. The dark current density J_d is one of the most important indicators of the noise figure of merit for photodetectors. Figure 8a shows the measured current density (J) of OPDs in dark and under light illumination (at 100 mW.cm^{-2}). J-V curves exhibit rectifying current voltage curves characteristic for diode behaviour. While J_d is greater than 1 µA.cm^{-2} for voltages between -1 and -2 V for 1:2 ratio, J_d is extremely low with 7.5 nA.cm^{-2} at -1 V and only increase to 17 nA.cm^{-2} at -2 V for 1:1 ratio demonstrating successful charge injection barrier and leading to rectification ratios at ±1 V of 92 and 294 respectively for blend ratio 1:2 and 1:1.[6,30] With our intentionally thick photo-active layers, we achieve a dark current 2 orders of magnitude lower than previously

reported 90 nm thick PM6:ITIC-4F BHJ-based OPDs.[28] An ultra-low dark current level is crucial and determines the limit of detection of photodetectors. The photocurrent density (J_{ph}) at the same bias reaches comparable values of 0.36-0.42 mA.cm^{-2} regardless of the blend ratio leading to ON/OFF ratios (J_{ph}/J_d) of 122 and 24 812 for ratio 1:2 and 1:1, respectively. The balanced 1:1 ratio also demonstrated better specifications with the highest responsivity $\Re$ of 159.6 mA.W^{-1} at 807 nm under -2 V (Figure S4, ESI†).

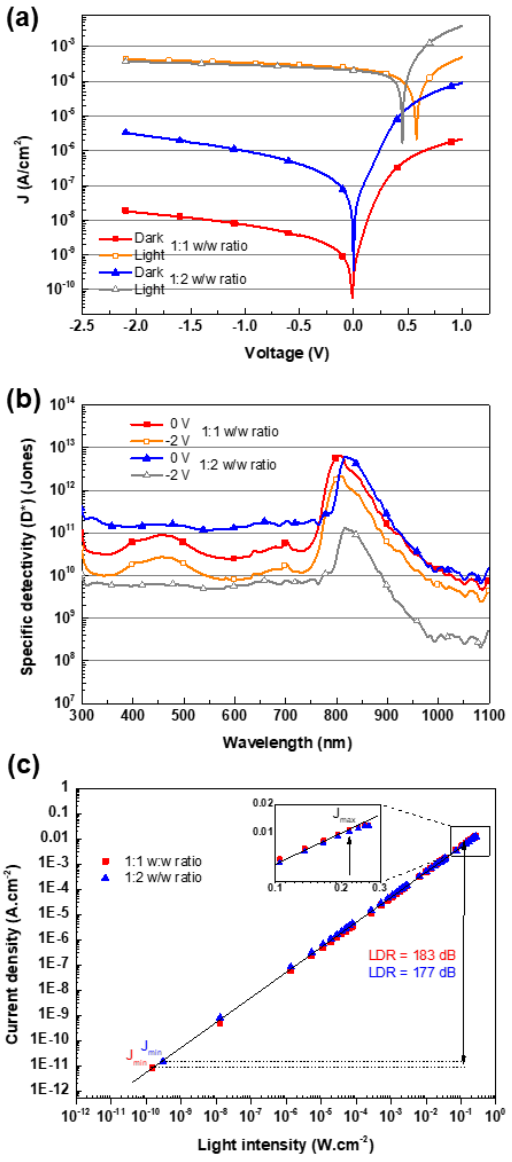

Figure 8: (a) Current-voltage characteristics of the optimized devices in dark and under light (100 mW.cm^{-2}), (b) Specific detectivity (D*) of the optimized devices under 0 V and -2 V and (c) Linear dynamic range (LDR) for the OPD measured at 0 V (pump wavelength ~810 nm).

Assuming that for organic photodetectors in which a reverse bias is applied, the dark current shot noise is generally considered the dominant contribution, the specific detectivity (D*) can be expressed as follows:[17,28,30]

$$D^* = \frac{\Re}{\sqrt{2qJ_d}} \qquad \text{(eq. 4)}$$

where q is elementary charge, J_d is the dark current density in $A.cm^{-2}$. In our case, the D* is calculated to be as high as ~ 6×10^{12} Jones for both ratios (Figure 8b). For 1:1 ratio, a slight decrease is calculated at -2 V with a value of 2.16×10^{12} Jones, while a drop to 1.2×10^{11} Jones is observed for the 1:2 ratio. The low dark current has a positive impact on the resulting D* of OPD in inverted structure with ratio 1:1. With D* over 10^{12} Jones, OPDs based on PM6:ITIC-4F in 1:1 ratio demonstrates comparable values as already reported for performing OPDs based on NFAs.[24,36]

It is also important for the photodiode to have a linear responsivity for a wide range of incident light intensities. This is expressed as a linear dynamic range (LDR), which is defined as:

$$LDR = 20\ \log_{10}\frac{J_{lin.max}(V)}{J_{lin.min}(V)} \qquad \text{(eq. 5)}$$

where J_{max} and J_{min} are the maximum and minimum values of the linear portion of the measurable photocurrent density, respectively. Upon illumination the current increases linearly with incident light intensity as shown in Figure 8c and Figure S17 for a bias voltage of 0 V and -2 V, respectively. It can be observed that the device current is limited by the dark current floor, whereas an expected deviation in the high intensity range is reached. A higher linear dynamic range (LDR) can be estimated at 0 V with 183 and 177 dB for 1:1 and 1:2 ratio, respectively. At -2 V, a slight decrease to 123 dB is observed. However, with LDR greater than 120 dB for both devices under reverse bias, this is consistent with typical values reported in other high-performance OPDs.[18,30,50,51]

Conclusions

We demonstrate a high-performance filter-free visible-blind near-infrared OPD utilizing the CCN effect originated from thick PM6:ITIC-4F BHJ films. A well-mixed and bi-continuous donor:acceptor morphology in thick films, crucial for the efficient carrier generation and transportation, is verified by GIWAXS and Raman. Applying a thermal annealing up to 200°C to PM6:ITIC-4F BHJ films generates a specific blend-induced crystallization with an evident face-on orientation for ITIC-4F based crystallites. A direct impact is observed on the charge transport capacity of BHJ layers at high annealing temperature with an imbalance between electron and hole mobility values. This results in a high charge electron mobility in the vertical direction of the OPD, and thus, efficient electron delocalization.

We demonstrated with this work that the concept of CCN is highly sensitive to mechanisms for manipulating the charge collection efficiency. After a careful optimization of the donor:acceptor ratio, film thickness, OPD architecture and thermal-annealing temperature of BHJs, a bottom-illuminated visible-blind near-infrared OPD is realized, showing a single-peak EQE response of 24.5% at a wavelength of 807 nm, along with a narrow FWHM of 42 nm. Additionally, employing a NFA acceptor in a balance 1:1 w/w ratio with PM6, considerably reduced the dark current of the OPDs, resulting in a higher specific detectivity of ~6×10^{12} Jones at 807 nm and a LDR>120 dB.

Author contributions

Q.E. and C.V.A. developed, fabricated and characterized the OPDs and the SCLC devices. Q.E. performed and analyzed the AFM measurements. Y.A.A.Q. performed the absorption analysis. C.R.H. performed the Raman analysis. T.K. and R.S. have performed the acquisition of GIWAXS patterns; N.Y. and C.V.A. have analyzed the data. C.V.A., J.A. and O.M. supervised the work. C.V.A. provided interpretation of experimental data and wrote the final manuscript including the contributions of all coauthors. All the authors contributed to the preparation of the manuscript and ESI.†

Conflicts of interest

There are no conflicts to declare.

Acknowledgements

This project has received funding by the French Research Agency (project ANR-18-CE04-0007-04 named BELUGA). Y.A.A.Q. and J.A. received funding from the French Research Agency (project ANR-17-CE05-0020-01 named NFA-15). The synchrotron radiation experiments were

performed at BL19B2 in Spring-8 with the approval of Japan Synchrotron Radiation Research Institute (JASRI) (Proposal No. 2021B1947, 2022A2069 and 2022A2063). C.V.A., J.A. and O.M. thank F. Jandard and S. Lavandier from CINaM (Electronics and instrumentation division) for their assistance in building the OPD measurement facilities and developing the acquisition software.

Note and references

1. Y. Wu, X. Li, Y. Wei, Y. Gu and H. Zeng, *Nanoscale*, 2018, **10**, 359.
2. X. Fu, N. Dong, G. Lian, S. Lv, T. Zhao, Q. Wang, D. Cui and C. Wong, *Nano Lett*.,2018, **18**, 1213.
3. Y. Xu and Q. Lin, *Appl. Phys. Rev.*, 2020, **7**, 011315.
4. Z. Lan, M.-H. Lee and F. Zhu, *Adv. Intell. Syst*., 2022, **4**, 2100167.
5. J. Vanderspikken, W. Maes and K. Vandewal, *Adv. Funct. Mater*., 2021, **31**, 2104060.
6. G. Simone, M. J. Dyson, S. C. J. Meskers, R. A. J. Janssen and G. H. Gelinck, *Adv. Funct. Mater*., 2019, **30**, 1904205.
7. S. Yoon, K. M. Sim and D. S. Chung, *J. Mater. Chem. C*, 2018, **6**, 13084.
8. M. Sun, Q. Fang, Z. Zhang, D. Xie, Y. Sun, J. Xu, W. Li, T. Ren and Y. Zhang, *ACS Appl. Mater. Interfaces*, 2018, **10**, 7231.
9. H. X. Sun, W. Tian, F. R. Cao, J. Xiong and L. Li, *Adv. Mater.*,2018, **30**, 1706986.
10. H. Ren, J.-D. Chen, Y.-Q. Li and J.-X. Tang, *Adv. Sci*., 2021, **8**, 2002418.
11. Z. Zhao, C. Xu, L. Niu, X. Zhang and F. Zhang, *Laser Photon. Rev.*, 2020, **14**, 2000262.
12. T. Yokota, P. Zalar, M. Kaltenbrunner, H. Jinno, N. Matsuhisa, H. Kitanosako, Y. Tachibana, W. Yukita, M. Koizumi and T. Someya, *Sci. Adv.*, 2016, **2**, e1501856.
13. R. Eckstein, N. Strobel, T. Rödlmeier, K. Glaser, U. Lemmer and G. Hernandez-Sosa, *Adv. Opt. Mater*., 2018, **6**, 1701108.
14. Y. Zhang, Y. Lang and G. Li, *EcoMat*., 2023, **5**, e12281.
15. H. Gao, Y. Sun, L. Meng, C. Han, X. Wan and Y. Chen, *Small*, 2023, **19**, 2205594.
16. Y. Wang, J. Kublitski, S. Xing, F. Dollinger, D. Spoltore, J. Benduhn and K. Leo, *Mater. Horiz*., 2022, **9**, 220.
17. X. Liu, Y. Lin, Y. Liao, J. Wu and Y. Zheng, *J. Mater. Chem. C*, 2018, **6**, 3499.
18. N. Strobel, N. Droseros, W. Köntges, M. Seiberlich, M. Pietsch, S. Schlisske, F. Lindheimer, R. R. Schröder, U. Lemmer, M. Pfannmöller, N. Banerji and G. Hernandez-Sosa, *Adv. Mater*., 2020, **32**, 1908258.
19. A. Armin, R. D. Jansen-van Vuuren, N. Kopidakis, P. L. Burn and P. Meredith, *Nat. Commun*., 2015, **6**, 6343.
20. A. Armin, A. Yazmaciyan, M. Hambsch, J. Li, P. L. Burn and P. Meredith, *ACS Photonics*, 2015, **2**, 1745.
21. A. Yazmaciyan, P. Meredith and A. Armin. *Adv. Optical Mater*., 2019, **7**, 1801543.
22. B. Xie, R. Xie, K. Zhang, Q. Yin, Z. Hu, G. Yu, F. Huang, Y. Cao, *Nat. Commun*., 2020, **11**, 2871.
23. Z. Lan, Y. S. Lau, Y. Wang, Z. Xiao, L. Ding, D. Luo and F. Zhu, *Adv. Optical Mater*., 2020, **8**, 2001388.
24. Q. Liu, S. Zeiske, X. Jiang, D. Desta, S. Mertens, S. Gielen, R. Shanivarasanthe, H.-G. Boyen, A. Armin and K. Vandewal, *Nat Commun*, 2022, **13**, 5194.
25. X. Du, T. Heumueller, W. Gruber, O. Almora, A. Classen, J. Qu, F. He, T. Unruh, N. Li and C. J. Brabec, *Adv. Mater*., 2020, **32**, 1908305.
26. X. Du, T. Heumueller, W. Gruber, A. Classen, T. Unruh, N. Li and C. J. Brabec, *Joule* 2019, **3**, 215.
27. P. Perkhun, W. Köntges, F. Pourcin, D. Esteoulle, E. Barulina, N. Yoshimoto, P. Pierron, O. Margeat, C. Videlot-Ackermann, A. Guerrero, J. Bisquert, R. R. Schröder, M. Pfannmöller, S. Ben Dkhil, J.-J. Simon and J. Ackermann, *Adv. Energy Sustain. Res*., 2021, **2**, 2000086.
28. T.H. Lee, Y. Dong, R.A. Pacalaj, S.Y. Park, W. Xu, J.-S. Kim and J.R. Durrant, *Adv. Funct. Mater*., **2022**, *32*, 2208001.
29. S. Ben Dkhil, M. Pfannmöller, R. R. Schröder, R. Alkarsifi, M. Gaceur, W. Köntges, H. Heidari, S. Bals, O. Margeat, J. Ackermann and C. Videlot-Ackermann, *ACS Appl. Mater. Interfaces,* **2018**, *10*, 3874.
30. M. Kielar, O. Dhez, G. Pecastaings, A. Curutchet and L. Hirsch, *Sci Rep.,* 2016*,* **6**, 39201.
31. S. Ben Dkhil, P. Perkhun, C. Luo, D. Müller, R. Alkarsifi, E. Barulina, Y. A. Avalos Quiroz, O. Margeat, S. T. Dubas, T. Koganezawa, D. Kuzuhara, N. Yoshimoto, C. Caddeo, A. Mattoni, B. Zimmermann, U. Würfel, M. Pfannmöller, S. Bals, J. Ackermann and C. Videlot-Ackermann, *ACS Appl. Mater. Interfaces,* 2020, **12**, 28404.
32. Y. A. Avalos-Quiroz, T. Koganezawa, P. Perkhun, E. Barulina, C.M. Ruiz, J. Ackermann, N. Yoshimoto and C. Videlot-Ackermann, *Adv. Electon. Mat.,* 2022, **8**, 2100743.
33. L. Ciammaruchi, O. Zapata-Arteaga, E. Gutiérrez-Fernández, J. Martin and M. Campoy-Quiles, *Mater. Adv*., **2020**, 1, 2846.
34. G. Han, T. Hu T and Y. Yi, *Adv. Mater*., 2020, **32**, 2000975.
35. C. M. Yang, P. Y. Tsai and S. F. Horng, *Appl. Phys. Lett*., 2008, **92**, 083504.

36. H. Bristow, P. Jacoutot, A. D. Scaccabarozzi, M. Babics, M. Moser, A. Wadsworth, T. D. Anthopoulos, A. Bakulin, I. McCulloch and N. Gasparini, *ACS Appl. Mater. Interfaces,* 2020, **12**, 48836.
37. K.-W. Tsai, G. Madhaiyan, L.-H. Lai, Y.-T. Hsiao, J.-L. Wu, C.-Y. Liao, C.-H. Hou, J.-J. Shyue and Y.-M. Chang, *ACS Appl. Mater. Interfaces,* 2022**,** *14*, 38004.
38. H. Cao, Y. Si, Y. Chen, Q. Liang and H. Wu. *ACS Appl. Mater. Interfaces,* 2022, **14**, 34926.
39. T. J. Aldrich, M. Matta, W. Zhu, S. M. Swick, C. L. Stern, G. C. Schatz, A. Facchetti, F. S. Melkonyan and T. J. Marks. *J. Am. Chem. Soc*., 2019, **141**, 3274.
40. Z. Li, S. Dai, J. Xin, L. Zhang, Y. Wu, J. Rech, F. Zhao, T. Li, K. Liu, Q. Liu, W. Ma, W. You, C. Wang and X. Zhan, *Mater. Chem. Front.,* 2018, **2**, 537.
41. T. J. Aldrich, S. M. Swick, F. S. Melkonyan and T. J. Marks, *Chem. Mater*., 2017, 29, 10294.
42. Y. Xiao, J. Yuan, G. Zhou, K. C. Ngan, X. Xia, J. Zhu, Y. Zou, N. Zhao, X. Zhan and X. Lu, *J. Mater. Chem. A*, 2021, 9, 17030.
43. T. Wang, R. Sun, M. Shi, F. Pan, Z. Hu, F. Huang, Y. Li and J. Min, *Adv. Energy Mater*., 2020, 10, 2000590.
44. Comprehensive Nanoscience and Technology*, Elsevier,* 1st Edition - October 29, 2010.
45. C. Li, M. Li, Z. Ni, Q. Guan, B. R. K. Blackman and E. Saiz, *J. R. Soc. Interface*, 2021, 18, 20210162.
46. A. Mahmood and J.-L. Wang, Sol. RRL, 2020, 4, 2000337.
47. H. Ko, S. Park, H. J. Son and D. S. Chung, *Chem. Mater.,* 2020, 32, 3219.
48. S. Wood, J. R. Hollis and J.-S. Kim, J. Phys. D: Appl. Phys., 2017, 50, 073001.
49. J.C. Blakesley, F. A. Castro, W. Kylberg, G. F.A. Dibb, C. Arantes, R. Valaski, M. Cremona, J. S.Kim and J.-S. Kim, *Org. Electronics,* 2014, 15, 1263.
50. J. Huang, J. Lee, J. Vollbrecht, V. V. Brus, A. L. Dixon, D. X. Cao, Z. Zhu, Z. Du, H. Wang, K. Cho, G. C. Bazan and T. Nguyen, *Adv. Mater*., 2019, 32, 1906027. 51.
51. C. Montenegro Benavides, S. Rechberger, E. Spiecker, M. Berlinghof, T. Unruh, M. Biele, O. Schmidt, C. J. Brabec and S. F. Tedde, *Org. Electron*., 2018, 54, 21.